

Deep Learning for direct Dark Matter search with nuclear emulsions

Artem Golovatiuk^{a,b,*}, Andrey Ustyuzhanin^{c,d}, Andrey Alexandrov^{a,b,d,e} and Giovanni De Lellis^{a,b}

^a*I.N.F.N. sezione di Napoli, Napoli 80126, Italy*

^b*Università degli Studi di Napoli Federico II, Napoli 80126, Italy*

^c*National Research University Higher School of Economics, Moscow 101000, Russia*

^d*National University of Science and Technology MISIS, Moscow 119049, Russia*

^e*Lebedev Physical Institute of the Russian Academy of Sciences, Moscow 119991, Russia*

ARTICLE INFO

Keywords:

Deep Learning
nuclear emulsion
Dark Matter search
direct detection

ABSTRACT

We propose a new method for discrimination of sub-micron nuclear recoil tracks from an instrumental background in fine-grain nuclear emulsions used in the directional dark matter search. The proposed method is based on the Deep Learning approach and uses a 3D Convolutional Neural Network architecture with parameters optimised by Bayesian search. Unlike previous studies focused on extracting the directional information, we focus on the signal/background separation exploiting the polarisation dependence of the Localised Surface Plasmon Resonance phenomenon. Comparing the proposed method with the conventional cut-based approach shows a significant boost in the rejection power while keeping the signal efficiency at the same level.

1. Introduction

Dark Matter (DM) is one of the remaining open questions of modern physics. While having numerous signatures of DM existence, we still have no evidence of the DM particles in the terrestrial experiments. Therefore it remains within the priorities for a fundamental understanding of the structure of our Universe.

Direct detection experiments are aiming at registering the signature of DM-nuclei scattering on the detector material. The range of DM particle masses and scattering cross-sections that can be probed in these experiments corresponds to Weakly Interacting Massive Particles (WIMPs) [1]. And within these experiments, some are trying to detect not only the fact of the recoil and its energy but also the recoil direction. This gives a possibility to probe additional features of the detected signal, as we expect a flow of DM particles directed from the Cygnus constellation [2], and better discriminate it from the background that is expected to be isotropic. Potentially, it is the only way to overcome the neutrino background, which is irreducible for other types of direct detection experiments.

Since the expected DM interaction rate in the Standard Halo model is very low [2], every direct detection experiment needs to reject all possible background. Many background reduction techniques are applied at the design stage (such as underground location, shielding, material screening and purification). However, some level of background contamination remains, and additional algorithmic background rejection is needed.

In this article, we present the Deep Learning (DL) approach to analysing the experimental data in the nuclear emulsion based directional detection experiment and compare it with a more conventional cut-based approaches adopted by the NEWSdm (Nuclear Emulsion for WIMP Search with direc-

tional measurement) experiment [3]: we repeat the analysis of the brightness peak evolution due to the change of the light polarisation in the optical microscope similar to [4, 5] and use the results of the elliptical shape analysis for optical images in unpolarised light from [6].

Our main goal is an effective reduction of the background contamination while keeping as much signal as possible. Experimentally, we can compensate lowered signal efficiency with higher statistics. On the other side, claiming a discovery in the search for very rare events requires extremely low levels of background. Additionally, we inspect the influence of the algorithmic event classification on the angular distributions in the sub-classes.

In sections 1.1 and 1.2 we describe the experimental setup and important physical effects used in the analysis. In sec. 2 we provide details on the data, the details of the analysis approaches are in sec. 3 and the performances are compared in sec. 4.

1.1. The NEWSdm experiment

The NEWSdm experiment [3] uses silver bromide (AgBr) crystals dispersed in the gelatin medium both as a target material and a tracking detector. The recoil nucleus leaves a track of activated crystals that are transformed into silver grains after chemical development, which further remain stable. The particular types of emulsions with fine crystal size of 75 nm and high granularity [7, 6] allow registering tracks with lengths shorter than 100 nm, preserving the directional information [8] in tracks with at least two grains.

The emulsion readout is performed with a custom-designed super-resolution optical microscope [9, 4]. This allows fast processing (e.g. compared to an X-ray microscope) of the emulsion volumes and allows to scale up the detector mass.

There remains some level of background contribution to the experimental tracks that needs to be analysed and discarded. Currently, two main background sources are intrinsic β radiation from ^{14}C isotopes in gelatin and random thermal excitations of the crystals (also called fog) that convert

*Corresponding author

✉ artem.golovatiuk@cern.ch (A. Golovatiuk)
ORCID(s): 0000-0002-7464-5675 (A. Golovatiuk)

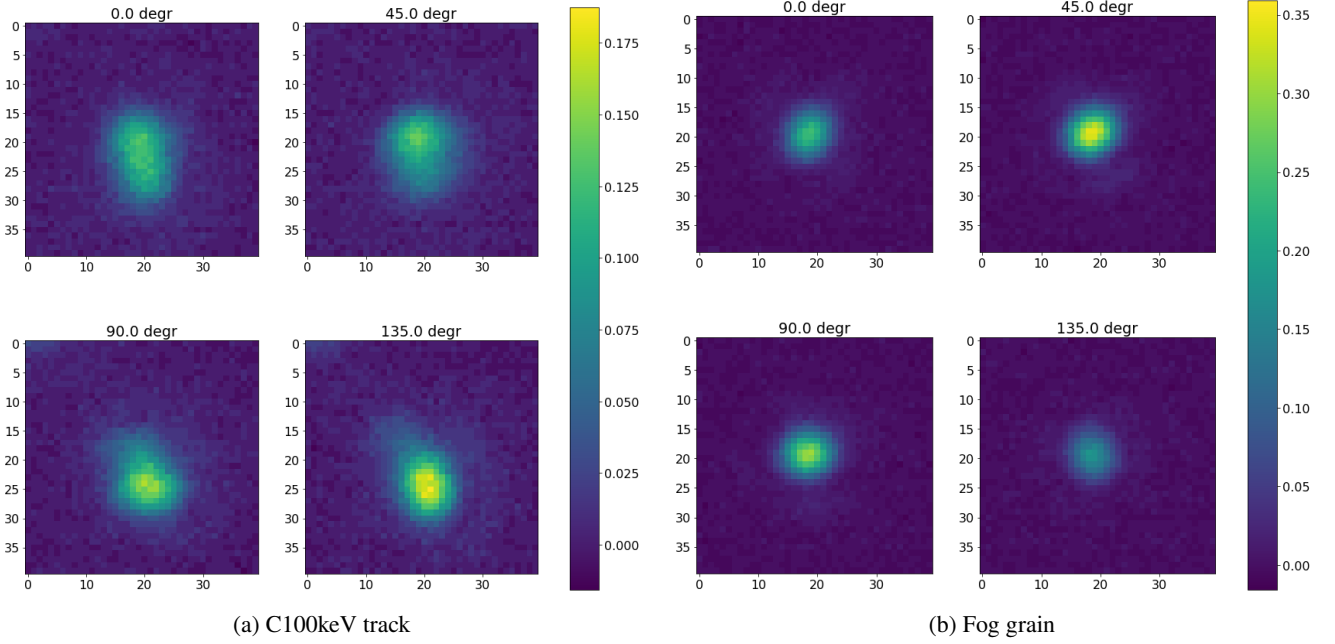


Figure 1: Examples of polarised images for one signal event and one background (fog) event.

into silver grains during chemical development. The background level due to the fog is expected to be orders of magnitude higher than that from β and therefore needs to be suppressed first.

1.2. Plasmon resonance effect

The plasmon resonance effect comes from the interaction of linearly polarised light with small metallic objects [9, 4]. The intensity of reflected light depends on the polarisation angle of the illuminating light if the object has a non-spherical shape. If we approximate the grain by an ellipsoid, then we get the resonant peak on a longer light wavelength with polarisation along the major axis and a shorter wavelength along the minor. We observe the variation of the reflected intensity with the rotation of the polarisation angle for a light with a fixed wavelength.

The silver grains have the form of randomly oriented filaments with the size of several tens of nanometers. Therefore, rotating the light polarisation produces resonant peaks at different angles for different grains. It causes the brightness peak of the image to shift between grains, producing a shift of the cluster barycenter. By studying the evolution of the image while rotating the polarisation direction, we can obtain additional insights into the internal structure of the track beyond the optical resolution. The barycenter shift is maximal when the grains' major axes are perpendicular and is close to zero when they are aligned. Therefore, it gives us a lower bound in estimating the real length of the corresponding tracks. The direction of the barycenter shift gives us the approximate angle of the original track's direction.

2. Experimental data

The data used in the analysis is currently purely experimental since Monte Carlo algorithms can not yet reproduce all the necessary physical processes altogether (track formation, chemical development, polarised light interaction). Emulsion samples are either exposed to a specific source or unexposed to anything (random fog). The most significant background contribution is expected from thermal fog and needs to be significantly reduced in the first place. Therefore, we study background rejection only on fog so far.

The expected signal of nuclear recoils from WIMPs is experimentally imitated by beams of Carbon ions of fixed energies. A combination of samples exposed to Carbon can be used to simulate the recoil spectrum of WIMPs with the desired mass value. The beam energies used in this study are 30 keV and 100 keV. Due to the high intensity of Carbon tracks in the exposed areas, a tiny fraction of background contamination in these samples can be neglected.

We have eight monochromatic images from an optical microscope for each track, obtained at different polarisation angles, uniformly covering the 180° period. Independent areas of the same emulsions were used to develop the algorithms (training) and cross-check the final performance (testing). The validation data is a separate part of the "train" scans, used not for training but for selecting the optimal algorithm or model. Figure 1 shows examples of microscope images taken at different polarisation angles for a Carbon 100 keV event (Fig. 1a) and for a fog event (Fig. 1b).

We apply some data cleaning prior to further analysis. We reject high event density areas, events with too small number of pixels, too low and too high brightness events, and non-isolated tracks (the ones with multiple optically re-

solved peaks). The applied cuts reject most of the events caused by the dust particles, high-density regions (caused by physical imperfections in the emulsion such as scratches) and fake events when combination of pixel noise in camera is identified as an event with low brightness and just several pixels. The same cleaning cuts are applied to all emulsion samples. This procedure is not expected to affect the tracks induced by WIMPs while reducing the background contamination.

The Carbon 30keV emulsion sample was partially damaged on the surface (scratches and dust contamination), but we manually selected the cleaner areas to avoid imperfections that may contribute to fake signal events.

2.1. Emulsion rotations

Due to residual vibrations of the microscope during the data acquisition, the measured barycenter shifts have some anisotropy. It is not expected to bring problems in background scanning since the latter is isotropic. However, the Carbon samples are exposed in a specific direction, and therefore the measurement anisotropy can interfere with it.

We manually rotate the emulsions and use a randomly shuffled mixture of events from the rotated scans in the DL training to make our analysis independent from the correlation between the beam direction and measurement anisotropy. We scan 4 independent areas for each Carbon sample: first with the default orientation (0° rotation), second rotated by 45° , third rotated by 90° and the last one with the default orientation to be used for the reproducibility cross-check of the results.

Comparing the angular distributions estimated from the image's barycenter movement due to the variation of the polarisation angle for samples scanned in the default orientation and rotated by 90° (Fig.2), one can see that measurement anisotropy dominates the directional information in the lower energy 30 keV sample, while we see the clear directional peak in 100 keV sample. However, it does not mean the directional information is not present in 30 keV sample. The lower beam energy produces shorter tracks and the scattering increases the angular distribution's width. Since barycenter shift analysis has measurement anisotropy, the small and wide peak can be hidden behind it and not visible in this method.

3. Analysis and methods

In the following we briefly describe the conventional analysis approach followed by a detailed description of the proposed DL-based one. Both approaches use the same microscopic images taken at different polarisation angles.

3.1. Conventional barycenter shift analysis

The barycenter shift produced by the variation of the polarisation angle can be used to try to distinguish single grains and tracks composed of more than one grain. Here we follow the approach similar to the one described in [4, 5].

Spherical silver nanoparticles (NP) should produce minimal barycenter shift as they are symmetric for the polarisa-

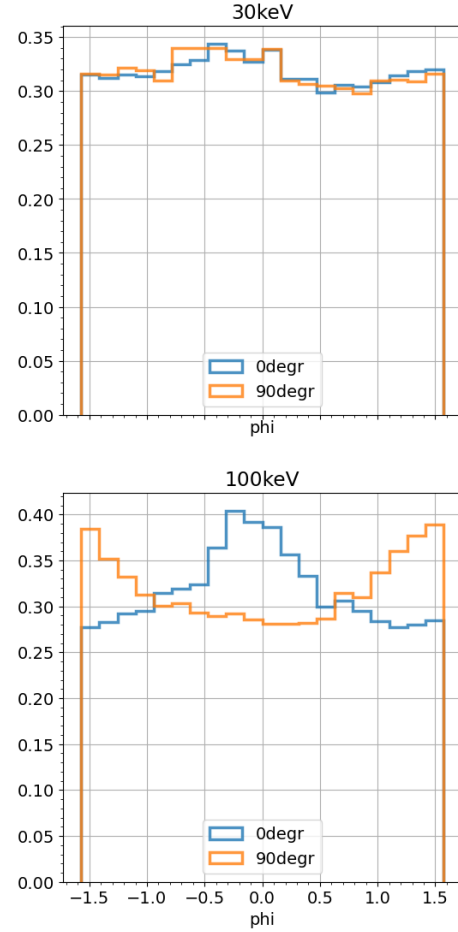


Figure 2: Comparison of the tracks angular distributions in rotated samples for different Carbon beam energies. Each histogram is normalised independently in a way that the area under the histogram integrates to 1.

tion direction. Data from an emulsion sample with NP can be used as a benchmark for single grains. We use emulsions with 75 nm AgBr crystal size while in [4, 5] used emulsion with the 45nm AgBr crystals, so the results should not be compared directly with those reported in these references. The nanoparticles we use are bigger as well to correspond better to the AgBr crystal size.

We identify the threshold on barycenter shift in a way that 95% of NPs give shifts shorter than the threshold on Figure 3. The threshold is set to 37.8 ± 1.0 nm. We then analyse the same distributions for Carbon and Fog samples to obtain signal efficiency and background rejection.

3.2. DL-based analysis

We study the machine learning approach to signal-background classification with Convolutional Neural Networks (CNNs) [10]. The main goal is the strongest achievable background rejection power while keeping good efficiency (percentage of signal that passes the selection). The study is performed in Python language [11] using Keras library [12] for building and using the network.

The network takes as an event input a 3D numeric array

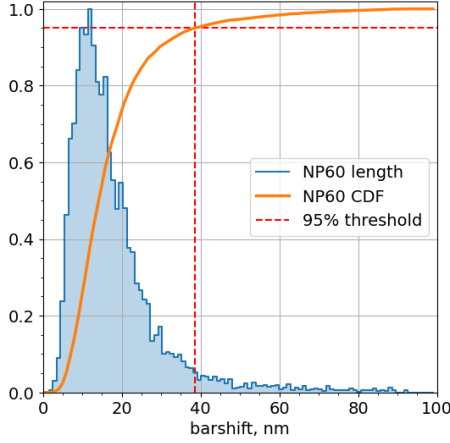


Figure 3: Barycenter shift distribution for 60nm spherical nanoparticles with the 95% quantile.

(2D polarised images stacked together to provide an additional dimension) and outputs 3 probability-like numbers (in the range from 0 to 1 and all 3 sum up to 1). The event outputs can be treated as pseudo-probabilities for corresponding classes: Carbon 30 keV, 100 keV and fog.

The realistic representation of the WIMP signal needs a combination of Carbon samples with different energies, so we want our network to identify all Carbon as a signal but preserve some knowledge about different energies. Therefore, we define the task as a multi-class problem with a mixed loss function (1).

$$L_{\text{balanced}} = L_{\text{multi}} + \mu_l L_{\text{binary}} \quad (1)$$

One part of the loss is categorical cross-entropy, defined in eq.(2), another is a binary cross-entropy (the same concept, but for two classes), that is multiplied by a hyper-parameter μ_l with a value optimised by the Bayesian search described in sec.3.2.3. The four classes in eq.(2) are Carbon 30 keV, 100 keV and fog, while for the binary case, we join all Carbons into a 'signal' class against 'background' (represented only by fog).

$$L_{\text{multi}} = \sum_i y_i \log(\bar{y}_i) \quad (2)$$

where \bar{y}_i is the vector of the output predictions of different classes for the specific event and y_i is the vector of the correct answers of the same shape, but with zeros corresponding to all classes except one.

To obtain a discrete answer from the classifier, we need to select a threshold on the probabilistic output. We define the criterion for the background rejection against efficiency balance and the threshold value on the validation set and then check the performance on the independent test scans. We choose a threshold value that provides the signal efficiency similar to the barycenter shift analysis. This way we can compare the improvement in background rejection.

3.2.1. Image preprocessing

We try to achieve several goals by preprocessing the images passed to the network: improving the convergence during training, reducing the impact of the instrumental noise and implying some physical knowledge into the data.

- **Image scaling.** For training convergence purposes, we scale images by the maximum pixel value before further processing. This value is the same for all images to avoid distortions by scaling.
- **Optical background subtraction.** The optical background around the track can contain distinguishable features not related to the event itself. Due to differences in production processes, Carbon-exposed and Fog samples have different thicknesses and event densities leading to slightly different image background brightness due to different properties of diffused light.

To avoid that the algorithm learns from the background brightness alone, we calculate the median brightness of each image and subtract the median value of the specific image from all its pixels (independently for every polarisation). Hence, the optical background brightness values are always centred around zero with slight variations (the camera noise amplitude is much lower than the scaling value). As a consequence, the contrast (signal-to-noise ratio) in the images is improved as well.

- **Periodic boundary conditions.** The polarisation angle has a period of 180° . If we add another rotation after the last, we will get the same polariser orientation as the first image. In order to account for this effect in our network, we add a copy of the first image after the last one, getting nine images in total.
- **Random rotations.** The directionality of the signal is an important feature, which we want to preserve in DL analysis. The initial background is isotropic, and in order to avoid the remaining background from adopting the same angular distribution as the signal, we apply algorithmic random rotations to every event. All nine images of the same track are rotated by the same angle to preserve correlations between polarisations.

3.2.2. Convolutional Neural Network

We are using the architecture inspired by ResNet [13, 14] and optimised for our specific task. The network consists of basic building blocks like convolution layers, SWISH activation functions [15], batch normalisation (BN) [16], max-pooling and dropout layers. The architecture is made of convolutions and groups of residual skip connections (identity shortcuts and convolution shortcuts as defined in [14]). The output is obtained from the softmax activation function with the corresponding number of classes (3 Carbon types and 1 fog), while for binary loss and final background rejection performance, the probabilities of signal classes are summed.

As we have important physical correlations stored in images for different polarisation angles, we consider a set of 9

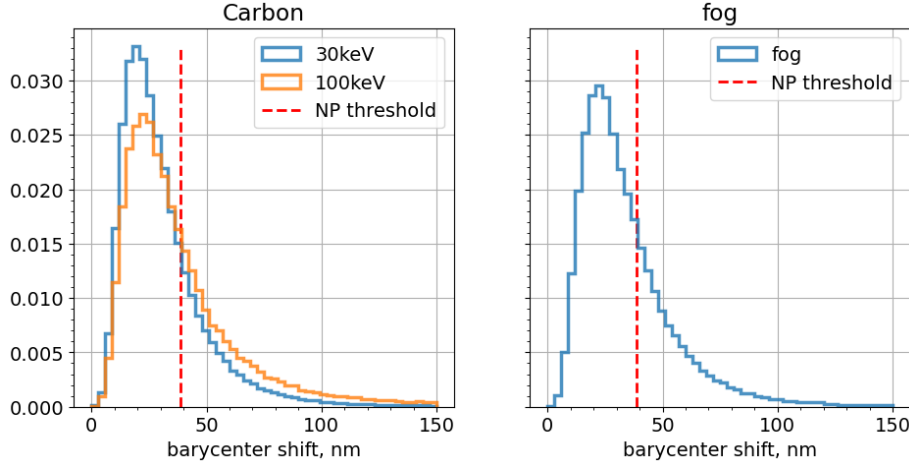


Figure 4: Barycenter shift distributions for tracks reconstructed in emulsions exposed to Carbon beams (left) and unexposed (right). The unexposed sample is representative of the random fog. NP threshold for short-long split is shown by the red dashed line.

images as one 3D image. We use 3D versions for all the CNN components. This allows the network to better find physical correlations along the "polarisation axis". The images are monochromatic, hence they have only one colour channel.

The detailed description of the NEWSnet architecture together with hyper-parameter values are provided in the Appendix A. The number of skip-connections, number of filters in the layers, regularisation parameters (dropout rates) and training parameters (such as learning rate) are optimised with Bayesian search [17].

3.2.3. Bayesian search

We use the Bayesian optimisation strategy to search for the optimal hyper-parameters set [17]. The Bayesian approach is an improved version of random search over the parameter space, where the probability distribution, from which the parameters are sampled, is not uniform but is updated using Gaussian Processes in order to optimise the goal function: area under the receiver operating characteristic (ROC) curve (AUC ROC) for binary classification in our case.

We implement this algorithm using the Scikit-optimize package [18]. The hyperparameters being optimised are:

- The dropout rates (3 dropout layers: before the residual blocks, in between and after final residual block).
- Number of convolution filters in the layers.
- Number of residual identity shortcuts after each residual convolutional shortcut [14].
- Proportion multiplier μ_{loss} for the combined loss (1).
- Learning rate (multiplier of the gradient step).
- β_1 and β_2 parameters of Adam optimizer [19] (decay rates for the 1st and 2nd momenta)
- Exponential decay rate for the learning rate.

For each set of parameters, we trained on half of the data and for fewer epochs to speed up the search, with 3-fold cross-validation, to obtain more robust results for the goal function. We take the parameter set corresponding to the best result on validation after 150 iterations of Bayesian search. The exact values and the constraints within which the search was performed are presented in the Appendix A.

4. Performance comparison

We compare both methods discussed in sec. 3 with the results reported in [6] for the same emulsion type, but obtained with elliptical shape analysis for optical images in unpolarised light. Each approach has its benefits and limitations, that are discussed in this section.

4.1. Barycenter shift thresholds

With the threshold derived from the analysis of NPs, we can split events into "long" and "short" tracks according to their barycenter shift values. Since we expect background to be mostly represented by single-grain events, while signal events need to be multi-grain to measure the direction, we can classify "short" track events as background. Figure 4 shows barycenter shift histograms for Carbon and fog samples with the threshold from Fig. 3.

The barycenter shifts follow the physical intuition for Carbon exposed samples, having in general longer track events for higher beam energies. However, it does not allow to separate them from the fog background effectively. The percentage of events surpassing the threshold (Tab. 1) is comparable for Carbon and fog samples and does not provide a way to effectively reduce the background, as it equally reduces the signal.

Figure 5 compares directions of the short and long track events. 100 keV Carbon events have a clear directional peak in the long tracks, while short follow the anisotropy pattern. 30 keV Carbon does not produce a clear direction even for long tracks and in the fog events, the anisotropy pattern is

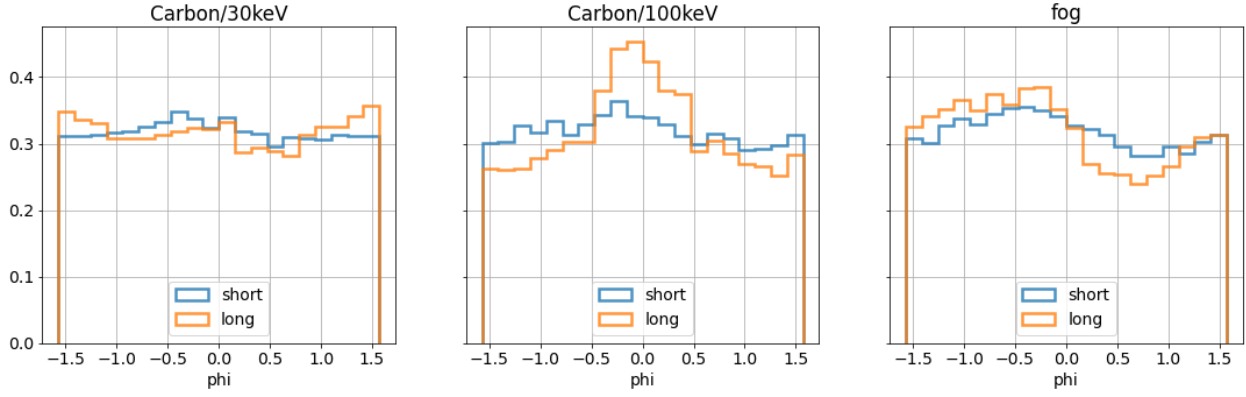


Figure 5: Angular distributions for the events with the barycenter shift longer and shorter than the threshold in different emulsion samples. Each histogram is normalised independently in a way that the area under the histogram integrates to 1.

Table 1

Comparison of the signal efficiencies and background rejection powers between barycenter shift analysis and NEWSnet on validation and test data. Last column contains the efficiencies of the shape analysis [6] performed on the same emulsion type.

	Barshift		NEWSnet		Shape analysis
	Validation	Test	Validation	Test	
Signal efficiency					
C30keV	$25.3 \pm 1.5\%$	$25.5 \pm 1.7\%$	$29.3 \pm 3.9\%$	$16.2 \pm 3.1\%$	$1.7 \pm 0.1\%$
C100keV	$38.0 \pm 1.8\%$	$38.2 \pm 1.2\%$	$36.5 \pm 3.4\%$	$37.4 \pm 3.3\%$	$29.7 \pm 0.7\%$
Background rejection power					
Fog	0.32 ± 0.02	0.39 ± 0.02	$(2.4 \pm 0.74) \cdot 10^{-3}$	$(4.2 \pm 1.3) \cdot 10^{-4}$	0.01

more significant in long tracks, as this anisotropy is expected to contribute to elongating the single-grain events.

4.2. Deep Learning selection

We visualise the performance as a ROC curve: the horizontal axis is True Positive rate (signal efficiency), the vertical axis is False Positive rate (the background rejection power). We took the model configuration with the highest AUC ROC on cross-validation in the Bayesian search (sec.3.2.3) and trained it on the entire training set for 60 epochs. We used networks from the last ten epochs of the training to obtain an ensemble to compute mean performance and confidence intervals on the results. The performance on the validation set is presented on Fig. 6.

To obtain a binary classifier, we select a threshold on the probabilistic output of the network on the validation set and cross-check the resulting performance on the test set (separate scanings of the independent areas of the same emulsions). We fix a threshold of 0.996 and present the results in Table 1. This threshold allows us to achieve a strong background rejection while preserving a significant part of the signal. We choose the threshold in order to achieve signal efficiency comparable with barycenter shift analysis results.

The changes in the performance between validation and test data are due to high threshold value, and therefore we require high confidence of the network to call event signal. The

contamination in the Carbon 30keV sample (mentioned in sec. 2) has a different pattern in different areas. Thus, the independent test area yields lower network output values, and the signal efficiency is decreased in this sample. Similarly, the network output is lower on the Fog test events, which gives us stronger rejection power. In general, this is acceptable behaviour since our primary goal is to reject anything that we suspect is not a signal.

The NEWSnet provides significant improvement in performance comparing to the shape analysis reported in the last column of the tab. 1. The background studied in [6] is represented by silver NP sample with high event density in order to simulate chance coincidences of multiple spherical particles located closer than the optical resolution. In that study they consider it similar to reference fog sample. More precise comparison can be achieved if both approaches are applied to the same emulsion sample.

We checked the same physical features of polarised images as in sec. 4.1 for the classification obtained by DL. Figure 7 show the barycenter shift and angular distributions for classified events. The "signal" distributions for the fog sample are less accurate due to the low amount of fog selected as a signal in test data (48 events).

The "signal" barycenter shifts are, in general, slightly longer but we do not observe a significant difference on fig. 7a. Therefore, DL selection does not use barycenter shift as a

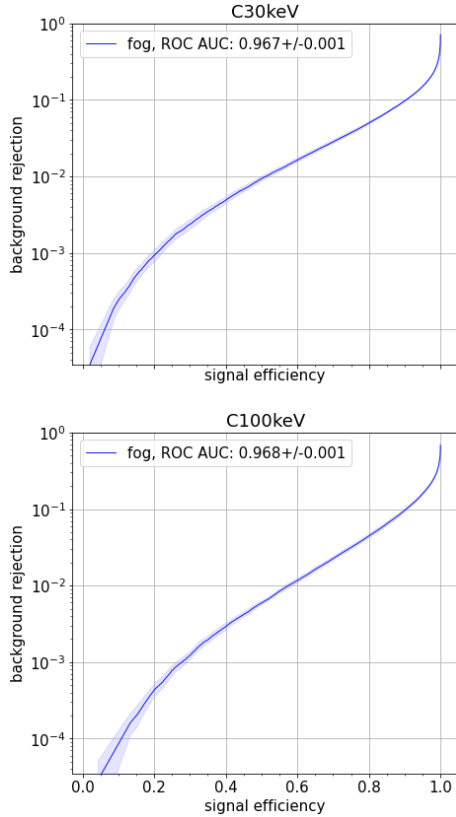


Figure 6: Signal efficiency against background rejection for different signal classes (Carbon beam energies) against Fog background.

distinctive feature. Angular distributions in fig. 7b show directional peak only in "signal" events in Carbon 100keV sample, similarly to fig. 5. The "signal" events in the fog sample do not tend to have a directional peak, however, a much bigger dataset is needed to get a more precise distribution.

The signal efficiencies of both barycenter shift analysis and the NEWSnet are higher than the ones with shape analysis. However, we are able to identify the directional peak in the signal only for 100 keV Carbon. While the shape analysis detects signal direction in the 30 keV Carbon, the efficiency is very low and comparable to the remaining background fraction. All these approaches need further improvements to identify direction and keep large fraction of signal for low recoil energies, as they correspond to smaller WIMP masses.

5. Conclusions

In the presented study, we compared conventional cut-based and DL-based approaches for background reduction in the nuclear emulsion WIMP search experiment. We used images from an optical microscope with a rotating polarising filter for the candidate events. The first approach is based on the displacement of the brightness peak due to resonant effects of polarised light reflected from non-spherical silver grains. It allows studying the estimated track length and di-

rection. The portion of the background passing the threshold is comparable to the portion of surviving signal and is of the order of 30%, and the directional peak in the signal is observed only for high Carbon beam energy.

The second approach is DL-based. We use 3D CNN to predict the track class. The final background rejection power is around 10^{-3} , and it is expected to get stronger on unknown data due to the strong threshold on the network's classifier output. The signal efficiency of our final model is similar to the cut-based approaches, while background reduction is orders of magnitude higher.

The events selected as a signal by the network show the directional peak only in the Carbon 100keV sample, which corresponds to a similar situation in the raw data. This means DL selection does not imply the directional information in the selected data, therefore this physical feature in the selected candidates can be considered intact and used for further analyses.

The NEWSnet can provide good background rejection and preselect a reduced number of candidates for further detailed study while preserving intact important physical features.

Acknowledgements

This work is supported by a Marie Skłodowska-Curie Innovative Training Network Fellowship of the European Commissions Horizon 2020 Programme under contract number 765710 INSIGHTS.

The research leading to these results has received funding from Russian Science Foundation under grant agreement n° 19-71-30020.

A. The NEWSnet architecture and parameters

The network starts with 3D convolutions, followed by the residual blocks defined in table 2, max pooling and dropout layers, finishing with a fully connected layer with softmax activation to produce the output predictions of different classes. The architecture with configurations for all the layers is presented in table 3. There was an additional third dropout layer during the Bayes optimisation before the final fully-connected one, but the optimal dropout rate for it turned out to be 0. The batch size is 256.

The parameter constrains and optimal values:

- The 3 dropout layers: before the residual blocks in range [0.1,0.4], the final value is 0.4; in the middle in range [0.3,0.8], the final value is 0.3; after the final residual block in range [0,0.4], the final value is 0.
- Number of convolution filters in the layers: for the residual blocks before the second dropout layer in range [32,64], the final value is 64; for the residual blocks after the second dropout layer in range [64, 128], the final value is 128.

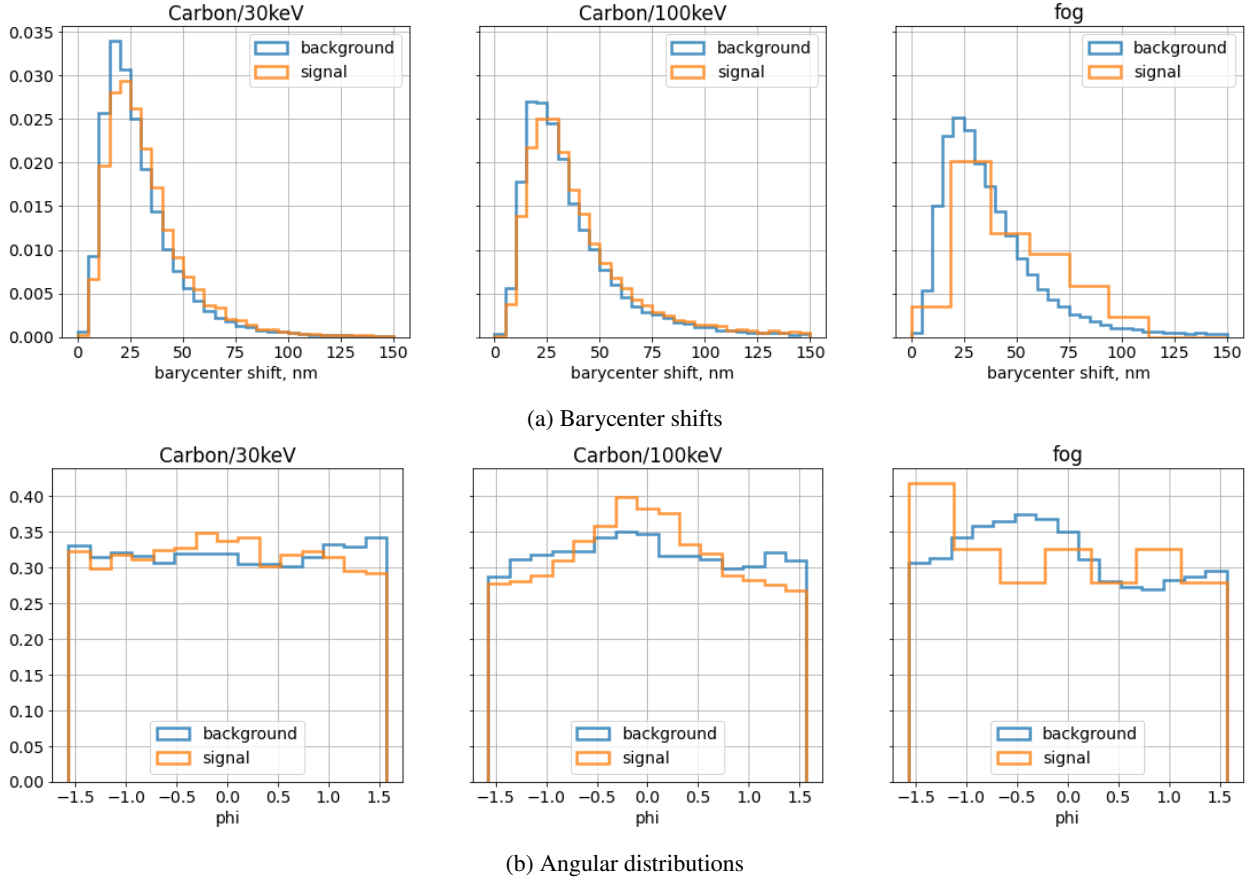


Figure 7: Physical features for the events selected as signal or background in different emulsion samples. Each histogram is normalised independently in a way that the area under the histogram integrates to 1.

- Number of residual identity shortcuts after each residual convolutional shortcut in range [0,3], the final value is 3.
- Proportion multiplier μ_{loss} for the combined loss (1) in range [0.01, 2], the final value is 0.53.
- Learning rate in range [10^{-5} , 3×10^{-3}], the final value is 6.5×10^{-4} .
- Parameters of Adam optimizer [19]: β_1 in range [10, 100], the final value is 10; β_2 in range [100, 1500], the final value is 100.
- Exponential decay rate for the learning rate in range [10^{-4} , 10^{-1}], the final value is 10^{-1} .

References

- [1] T. M. Undagoitia, L. Rauch, Journal of Physics G: Nuclear and Particle Physics 43 (2015) 13001.
- [2] T. M. Undagoitia, L. Rauch, Journal of Physics G: Nuclear and Particle Physics 43 (2015) 13001.
- [3] A. Aleksandrov, A. Anokhina, T. Asada, D. Bender, I. Bodnarchuk, A. Buonaura, S. Buontempo, M. Chernyavskii, A. Chukanov, L. Consiglio, Others, arXiv preprint arXiv:1604.04199 (2016).
- [4] A. Alexandrov, T. Asada, G. D. Lellis, A. D. Crescenzo, V. Gentile, T. Naka, V. Tioukov, A. Umemoto, Scientific Reports 10 (2020) 1–12.
- [5] A. Umemoto, T. Naka, A. Alexandrov, M. Yoshimoto, Progress of Theoretical and Experimental Physics 2019 (2019) 063H02.
- [6] A. Umemoto, T. Naka, T. Nakano, R. Kobayashi, T. Shiraishi, T. Asada, Progress of Theoretical and Experimental Physics 2020 (2020) 103H02.
- [7] T. Asada, T. Naka, K.-i. Kuwabara, M. Yoshimoto, Progress of Theoretical and Experimental Physics 2017 (2017) 063H01.
- [8] A. Alexandrov, G. D. Lellis, A. D. Crescenzo, A. Golovatiuk, V. Tioukov, Journal of Cosmology and Astroparticle Physics 2021 (2021) 47.
- [9] A. Alexandrov, T. Asada, L. Consiglio, G. D. Lellis, A. D. Crescenzo, N. D. Marco, S. Furuya, K. Hakamata, M. Ishikawa, T. Katsuragawa, Others, Nuclear Instruments and Methods in Physics Research Section A: Accelerators, Spectrometers, Detectors and Associated Equipment 824 (2016) 600–602.
- [10] Y. LeCun, B. Boser, J. S. Denker, D. Henderson, R. E. Howard, W. Hubbard, L. D. Jackel, Neural computation 1 (1989) 541–551.
- [11] P. project, Python, 2021. URL: <https://www.python.org/downloads/release/python-3710/>.
- [12] F. Chollet, et al., Keras, 2019. URL: <https://github.com/keras-team/keras/>.
- [13] K. He, X. Zhang, S. Ren, J. Sun, in: Proceedings of the IEEE conference on computer vision and pattern recognition, pp. 770–778.
- [14] K. He, X. Zhang, S. Ren, J. Sun, in: European conference on computer vision, pp. 630–645.
- [15] P. Ramachandran, B. Zoph, Q. V. Le, arXiv preprint arXiv:1710.05941 (2017).
- [16] J. Bjorck, C. Gomes, B. Selman, K. Q. Weinberger, arXiv preprint arXiv:1806.02375 (2018).
- [17] J. Snoek, H. Larochelle, R. P. Adams, arXiv preprint arXiv:1206.2944

Table 2

Residual building blocks with (N,N,4N) filters. Strides are 1 when not specified otherwise.

Residual block: identity shortcut [13]	
$1 \times 1 \times 1$ 3D Conv., N filters, BN, SWISH	
$3 \times 3 \times 3$ 3D Conv., N filters, BN, SWISH	Identity path
$1 \times 1 \times 1$ 3D Conv., 4N filters, BN	
Addition of paths SWISH	
Residual block: convolution shortcut [14]	
$1 \times 1 \times 1$ 3D Conv., 2 stride, N filters, BN, SWISH	
$3 \times 3 \times 3$ 3D Conv., N filters, BN, SWISH	$3 \times 3 \times 3$ 3D Conv., 2 stride, 4N filters, BN
$1 \times 1 \times 1$ 3D Conv., 4N filters, BN	
Addition of paths SWISH	

Table 3

Final NEWSnet architecture.

$3 \times 3 \times 3$ 3D Conv., 32 filters, BN, SWISH
 $3 \times 3 \times 3$ 3D Conv., 64 filters, BN, SWISH
 MaxPooling 3D
 Dropout 0.4 rate
 Residual convolution block (64,64,256) filters
 Residual identity block (64,64,256) filters
 Residual identity block (64,64,256) filters
 Residual identity block (64,64,256) filters
 MaxPooling 3D
 Dropout 0.3 rate
 Residual convolution block (128,128,512) filters
 Residual identity block (128,128,512) filters
 Residual identity block (128,128,512) filters
 Residual identity block (128,128,512) filters
 Flatten
 FC layer 4 units
 Softmax

(2012).

- [18] T. Head, MechCoder, G. Louppe, I. Shcherbatyi, Others, scikit-optimize, 2020. URL: <https://github.com/scikit-optimize/scikit-optimize/>.
- [19] D. P. Kingma, J. Ba, arXiv preprint arXiv:1412.6980 (2014).